Boundary-Layer Meteorol (2007) 124:335–360
DOI 10.1007/s10546-007-9169-6

ORIGINAL PAPER

Quadrant analysis of the scalar and momentum fluxes in the stable marine atmospheric surface layer

George D. Katsouvas · Costas G. Helmis · Qing Wang

Received: 3 August 2006 / Accepted: 12 February 2007 / Published online: 13 March 2007

Abstract The quadrant technique, a conditional sampling approach that allocates Reynolds stresses into four different types of events (ejections or bursts, sweeps, inward interactions and outward interactions), is applied to stable marine atmospheric boundary-layer data, collected in the framework of the Coupled Boundary Layer Air—Sea Transfer, Low wind component experiment at Nantucket Island, Massachusetts, USA. The general properties of both scalar and momentum transport are analyzed under the scope of quadrant analysis experimentally and theoretically. It is shown that the third-order Gram–Charlier series is necessary and even sufficient in most of the cases, in describing the experimental time and flux contributions of each quadrant to the total transfer, for both scalar and momentum transport, while the ability of the Gaussian distribution is limited to outlining the general pattern of these quantities. Moreover, a threshold value is applied to the conditional analysis, separating the most important events from the less significant ones and the sensitivity of the flux and especially the time fraction of each quadrant on the choice of this value is presented and discussed. Also, a set of numerically extracted equations, completing the analytical relations, is derived, enabling the prediction of the time and flux fractions of each quadrant, for a wide range of correlation coefficient and threshold values. Finally, the sensitivity of the analysis to the atmospheric stability and the Reynolds averaging scales showed that correlated and uncorrelated motions tend to balance for increasingly stable conditions and/or for large time scales.

G. D. Katsouvas · C. G. Helmis (✉)
Department of Applied Physics, Faculty of Physics,
University of Athens,
University Campus, Building Phys.-5,
Athens 15784, Greece
e-mail: chelmis@phys.uoa.gr

Q. Wang
Department of Meteorology,
Naval Postgraduate School,
Monterey, CA, USA

Keywords Gaussian distribution · Gram–Charlier series · Marine atmospheric boundary layer · Momentum fluxes · Quadrant analysis · Scalar fluxes

1 Introduction

Quadrant analysis, among other conditional sampling techniques, has been extensively used in the study and description of turbulent shear flows near rough and smooth boundaries (Antonia 1981, Willmarth and Lu 1974). This technique allocates momentum and/or scalar transport into four different types of events (ejections or bursts, sweeps, inward interactions and outward interactions), which can be considered as the foundation of coherent structures in turbulent flow (Cantwell 1981, Robinson 1991). Direct comparisons with turbulent flow visualization have shown that the quadrant technique exhibits great reliability in providing correct quantitative data in support of the visual observations. Bogard and Tiederman (1986) evaluated the effectiveness of various burst detection algorithms (VITA, Quadrant, TRAPV, U-level, Positive slope and VITA with slope) in comparison with flow visualization and concluded that: "the quadrant technique has the greatest reliability with a high probability of detecting the ejections and a low probability of false detections". However, the effectiveness of each of the detection algorithms, including the quadrant analysis, exhibits a high dependence on operational parameters, such as the threshold level or the averaging time. This fact, combined with the use of different techniques under different field or laboratory conditions, makes the comparison between the results uncertain and the unification of the conclusions and interpretations difficult.

A brief outline of the historical progress of turbulent boundary-layer structure research can be found in Robinson (1991). The turbulent fluxes, for smooth and rough open channels (Nakagawa and Nezu 1977), or smooth and rough wind tunnels (Raupach 1981), or within the atmospheric surface layer (ASL) for different terrain types, such as forests (Hogstrom and Bergstrom 1996, Maitani and Shaw 1990, Bergstrom and Hogstrom 1989), bare soil (Maitani and Ohtaki 1987, Katul et al. 1997), rice paddy (Maitani and Ohtaki 1987), low vegetation (Hogstrom and Bergstrom 1996, Katul et al. 1997), corn and wheat (Shaw et al. 1983, Shaw 1985), have been often described in terms of the quadrant analysis. While the study of momentum flux structure in the ASL has received considerable attention, much less work has been done for the scalar transport (heat or humidity) and especially over the ocean. However, the existence of large-scale motions (Boppe et al. 1999) and the grouping of ejections into larger structures (Boppe and Neu 1995) have been verified in the marine ASL, through the quadrant analysis of the $u'w'$ covariance.

Our work aims at the experimental and theoretical study of the marine atmospheric boundary-layer (MABL) structure, under the scope of quadrant analysis. An attempt to describe both scalar and momentum fluxes uniformly, under the same mathematical relations is made. Also, the sensitivity of the analysis to the threshold level, the Reynolds averaging time and the atmospheric stability is examined and discussed.

2 Experimental site and instrumentation

The quadrant technique is applied to stable marine ASL data, collected in the framework of the Coupled Boundary Layer Air—Sea Transfer, Low wind component

experiment (CBLAST-Low), during the 2003 experimental campaign (from 30 July 2003 to 27 August), at Nantucket Island, Massachusetts, USA. The experimental site was located on the south coast of the island, at a distance of 94 m from the waterfront. The terrain surrounding the site is relatively flat, except for the eastern and south-eastern directions, where elevated sand dunes exist.

On a 20 m high meteorological mast there were two levels (10 and 20 m) of high frequency (20 Hz) sampling sonic anemometers for three-dimensional wind components (u, v and w) and virtual temperature (T) measurements, and a fast hygrometer at 20 m for water vapour (q) and carbon dioxide (CO_2) concentration measurements. These high frequency measurements yield estimates of momentum ($\overline{u'w'}$ and $\overline{v'w'}$), heat ($\overline{w'T'}$), humidity ($\overline{w'q'}$) and CO_2 fluxes through the eddy correlation method, for 10-min time intervals. There were also measurements of the mean wind, temperature and relative humidity (RH), with slow response sensors, at 5, 10 and 20 m heights for 10-min time intervals, with a sampling frequency of 1 Hz. Soil temperatures at 0.1 and 0.3 m below the surface were also measured at the foot of the 20-m meteorological mast. About 10 m to the north of this mast was a 2-m high mast (installed by Woods Hole Oceanographic Institution) on a tripod, instrumented to measure air temperature, RH, wind speed and direction, air pressure, precipitation and downward solar radiation at 1-min time intervals. More details on the experimental site and instrumentation can be found in Wang et al. (2004).

Only the dataset that refers to the MABL will be analyzed. It should be mentioned that this experimental site was chosen because the wind direction was predominantly south to south-west. As will be explained in the next section, the marine data correspond to measurements taken for wind directions in the sector 200° to 250°.

3 Data correction and processing

A set of data correction/selection procedures was applied to the whole dataset before the analysis. The first one was the data correction due to the axis tilt of the sonic anemometer. To do this, 10-min averages of the three wind components (u_s, v_s and w_s), calculated in the sonic coordinate system, for a 28-day time period (the whole experimental period), were utilized. This correction was performed in order to eliminate the dependence of the vertical wind component $\overline{w_s}$ on both horizontal wind components, $\overline{u_s}$ and $\overline{v_s}$, which is expected to arise due to the tilt of the anemometer from the true vertical (Mahrt et al. 1996). The following relation describes this dependence:

$$\overline{w_s} = a_0 + a_1\overline{u_s} + a_2\overline{v_s}. \tag{1}$$

Multiple regression was used to solve for the unknown coefficients a_0, a_1 and a_2, by performing a least squares fit to Eq. 1. Nullification of the coefficients a_1 and a_2 was achieved by the rotation of the anemometer's coordinate system. Two rotations were applied: (a) a rotation around the v-axis (pitch angle ϑ_1), in order to eliminate the dependence of $\overline{w_s}$ on $\overline{u_s}$, and (b) a rotation around the u-axis (roll angle ϑ_2), in order to eliminate the dependence of $\overline{w_s}$ on $\overline{v_s}$. In addition to the rotation, the correction of the data is completed by the subtraction of a_0. The transformation is applied to the instantaneous wind speed components.

Although the calculated rotation angles were relatively small ($\vartheta_1 = -0.063°$ and $\vartheta_2 = -2.486°$), the influence of the correction was quite important for certain wind direction sectors. Suggestively, the errors on the computed friction velocity exceeded

50% in some cases, and a similar influence of the tilt correction was reported by Mahrt et al. (1996) for the drag coefficient. However, the errors for the wind sector that corresponds to the pure MABL (200°–250°, as will be discussed later) are very small, due to the orientation of the anemometer.

A third rotation was applied to the tilt corrected data, around the z-axis, in order to align the x-axis to the 10-min averaged vector of the horizontal wind. Thus, hereinafter u coincides with the alongwind component, v is the wind component normal to the mean wind direction and w is the vertical wind component.

Since an internal boundary layer (IBL) is expected to develop due to flow from the land, the data concerning the MABL were carefully separated from the whole dataset, for the 20-m height level. The marine dataset was defined through a detailed examination of the measured momentum and heat fluxes, and the stability parameter ($-z/L$, where L is the Obukhov length and z is the height) time series at both 10-m and 20-m levels. It was clarified that the wind sector from 200° to 250° corresponds to a pure MABL.

From total 28 days of continuous data, only the marine data that correspond to stable conditions are analyzed (e.g. 713 10-min periods).

4 Theoretical background

4.1 Quadrant analysis

Quadrant analysis provides information on the processes of turbulent production and transfer by sorting the instantaneous values of the Reynolds stress, $u'w'$ and $v'w'$, as well as of scalar transport ($w'T'$ and $w'q'$), into four categories according to the sign of the two fluctuating components. The quadrants for $u'w'$ in the (u',w')-plane are numbered conventionally, as follows (Shaw et al. 1983):

quadrant 1 (Q_1): $u' > 0, w' > 0$ outward interaction,
quadrant 2 (Q_2): $u' < 0, w' > 0$ ejection or burst,
quadrant 3 (Q_3): $u' < 0, w' < 0$ inward interaction,
quadrant 4 (Q_4): $u' > 0, w' < 0$ sweep or gust.

Quadrants 2 and 4 both correspond to the downward transport of momentum (correlated motions) and quadrants 1 and 3 represent upward transfer (uncorrelated motions). The hyperbola:

$$|u'w'| = H|\overline{u'w'}| \tag{2}$$

defines a fifth area in the (u',w')-plane for the conditional analysis and it is used to separate the most important events, with large values of $|u'w'|$, from the less important ones. By the term "event" a single occurrence at a specific quadrant is implied. According to Raupach (1981) a stress fraction $S_{i,H}$ is defined as:

$$S(i,H) = \frac{< w'u' >_{i,H}}{\overline{w'u'}}, \tag{3}$$

where the subscript i corresponds to the quadrant number and

$$< u'w' >_{i,H} = \lim_{T\to\infty} \frac{1}{T} \int_0^T u'w'(t) I_{i,H}(t) \mathrm{d}t \tag{4}$$

is a conditional average, since the term $I_{i,H}$ is the following conditioning function:

$$I_{i,H} = \begin{cases} 0, \\ \text{if } u'w' \text{ is in quadrant } i \text{ and } |u'w'| \geq H|\overline{u'w'}| \\ 1, \text{ otherwise.} \end{cases} \tag{5}$$

From the definition of the stress fraction we obtain:

$$\sum_{i=1}^{4} S_{i,0} = 1. \tag{6}$$

The total time that is occupied by a specific quadrant within the Reynolds stress averaging time is called the fractional time $T_{i,H}$, defined as:

$$T_{i,H} = \frac{1}{T} \int_0^T I_{i,H}(t)\, \mathrm{d}t. \tag{7}$$

The ratio of upward to downward momentum transfer (E):

$$E = \frac{S_{1,0} + S_{3,0}}{S_{2,0} + S_{4,0}} \tag{8}$$

was introduced by Shaw et al. (1983) and was called the exuberance, since it represents a measure of the upward momentum transfer, which is counter to the overall downward flux, expressing the exuberant nature of the flow.

The definitions of the four quadrants for the scalar transport ($w'T'$ and $w'q'$, where T is the sonic virtual temperature and q the specific humidity) are altered compared to previous definitions for momentum flux (see also Katul et al. 1997, for the quadrant nomenclature for scalar transport). For example, the quadrants for $w'T'$ in the (w',T')-plane are named as follows:

quadrant 1 (Q_1): $w' > 0$, $T' > 0$ ejections,
quadrant 2 (Q_2): $w' < 0$, $T' > 0$ inward interactions,
quadrant 3 (Q_3): $w' < 0$, $T' < 0$ sweeps,
quadrant 4 (Q_4): $w' > 0$, $T' < 0$ outward interactions.

Regarding the heat transfer ($w'T'$), it is worth noting that ejections and sweeps become the dominant quadrants for unstable conditions, while for stable stratification the interaction quadrants prevail, consistent with the upward and downward overall heat transfer, respectively. It should be mentioned that the same definitions of the stress and time fractions that were given previously for Reynolds stress are also applied to the scalar quantities.

4.2 Conditional probability distribution of the Reynolds stress

In order to quantify the departures of the joint probability density distributions of turbulent velocities from Gaussianity, we consider the joint probability distribution of the Gram-Charlier type (Appendix A: Eqs. 26–36). Based on the third-order Gram–Charlier distribution and by using conditional calculations (Nakagawa and Nezu 1977), the contribution to the Reynolds stress from each component of the quadrant analysis can be predicted (Appendix A: Eqs. 37–52). Two different parts of the time fraction $T_{i,H}$ and the flux or stress fraction $S_{i,H}$ of each quadrant (i) are considered: (a)

the *'Gaussian'* part, and (b) the *'Residual'* part. The following relations describe this separation:

$$T_{i,H} = Tgauss^{-}{}_{i,H}(R) + Tres^{-}{}_{i,H}(R, S^{-}, D^{-}), \tag{9}$$

for $i = 2, 4$

$$T_{i,H} = Tgauss^{+}{}_{i,H}(R) + Tres^{+}{}_{i,H}(R, S^{+}, D^{+}), \tag{10}$$

for $i = 1, 3$

$$S_{i,H} = Sgauss^{-}{}_{i,H}(R) + Sres^{-}{}_{i,H}(R, S^{-}, D^{-}), \tag{11}$$

for $i = 2, 4$

$$S_{i,H} = Sgauss^{+}{}_{i,H}(R) + Sres^{+}{}_{i,H}(R, S^{+}, D^{+}), \tag{12}$$

for $i = 1, 3$.

The functions: $Tgauss^{-}{}_{i,H}(R)$, $Tgauss^{+}{}_{i,H}(R)$, $Sgauss^{-}{}_{i,H}(R)$ and $Sgauss^{+}{}_{i,H}(R)$ express the *'Gaussian'* part of the time and stress contributions of each quadrant, which is only related to the correlation coefficient (R), while the functions: $Tres^{-}{}_{i,H}\left(R, S^{-}, D^{-}\right)$, $Tres^{+}{}_{i,H}\left(R, S^{+}, D^{+}\right)$, $Sres^{-}{}_{i,H}\left(R, S^{-}, D^{-}\right)$ and $Sres^{+}{}_{i,H}\left(R, S^{+}, D^{+}\right)$ express the non-*'Gaussian'* part (residual functions) of the corresponding contributions. The residual functions are related to the skewness (S^{+}, S^{-}) and diffusion factors (D^{+}, D^{-}), which are involved in the turbulent energy budget in the term representing turbulent energy diffusion. These third-order terms are defined in Appendix A and can be seen as a measure of the skewness or intermittency of the distribution. The analytical relations for these functions are given below:

$$Tres^{-}{}_{i,H}(R, S^{-}, D^{-}) = -\frac{\mathrm{e}^{H(-1+R)}\left(3D^{-}H(-1+R) + (1 + H(-1+R) + R)S^{-}\right)}{6\sqrt{2\pi}(-1+R)}, \tag{13}$$

$$Tres^{+}{}_{i,H}(R, S^{+}, D^{+}) = -\frac{\mathrm{e}^{-H(1+R)}\left(3D^{+}H(1+R) + (-1 + H + R + RH)S^{+}\right)}{6\sqrt{2\pi}(-1+R)}, \tag{14}$$

$$Sres^{-}{}_{i,H}(R, S^{-}, D^{-}) = \frac{\mathrm{e}^{H(-1+R)}\left(3D^{-}(1 + H(-1 + H(-1+R))(-1+R)) + (-R + H(-1+R)(H(-1+R) + R))S^{-}\right)}{6\sqrt{2\pi}R}, \tag{15}$$

$$Sres^{+}{}_{i,H}(R, S^{+}, D^{+}) = -\frac{\mathrm{e}^{-H(1+R)}\left(3D^{+}(1 + H(1+R)(1 + H + HR)) + (R + H(1+R)(H + R + HR))S^{+}\right)}{6\sqrt{2\pi}R}. \tag{16}$$

For the special case of a zero threshold value (H) these equations are reduced to the following expressions:

$$Tres^{-}{}_{i,0}(R, S^{-}, D^{-}) = -\frac{S^{-}}{6\sqrt{2\pi}}, \tag{17}$$

$$Tres^{+}{}_{i,0}(R, S^{+}, D^{+}) = -\frac{S^{+}}{6\sqrt{2\pi}}, \tag{18}$$

$$Sres^{-}{}_{i,0}(R, S^{-}, D^{-}) = -\frac{-3D^{-} + RS^{-}}{6\sqrt{2\pi}R}, \tag{19}$$

$$Sres^{+}{}_{i,0}(R, S^{+}, D^{+}) = -\frac{3D^{+} + RS^{+}}{6\sqrt{2\pi}R}. \tag{20}$$

The analytical relations for the *'Gaussian'* part of the stress (*Sgauss*) and time contribution (*Tgauss*) of each quadrant can be explicitly approximated only for the threshold value $H = 0$, as follows:

$$Tgauss^{-}{}_{i,0}(R) = \begin{cases} -\frac{\sqrt{1-R^2}(\pi+2\mathrm{ArcSin}(R))}{4\pi\sqrt{-1+\frac{1}{R^2}}R}, \\ R < 0, \\ \frac{1}{2} - \frac{\sqrt{1-R^2}(\pi-2\mathrm{ArcSin}(R))}{4\pi\sqrt{-1+\frac{1}{R^2}}R}, \\ R > 0, \end{cases} \tag{21}$$

$$Tgauss^{+}{}_{i,0}(R) = \begin{cases} \frac{1}{2} + \frac{\sqrt{1-R^2}(\pi+2\mathrm{ArcSin}(R))}{4\pi\sqrt{-1+\frac{1}{R^2}}R}, \\ R < 0, \\ \frac{\sqrt{1-R^2}(\pi-2\mathrm{ArcSin}(R))}{4\pi\sqrt{-1+\frac{1}{R^2}}R}, \\ R > 0, \end{cases} \tag{22}$$

$$Sgauss^{-}{}_{i,0}(R) = \begin{cases} \frac{\sqrt{1-R^2}\left(-\pi+2\sqrt{-1+\frac{1}{R^2}}-2\mathrm{ArcSin}(R)\right)}{4\pi\sqrt{-1+\frac{1}{R^2}}R}, \\ R < 0, \\ \frac{1}{2} - \frac{\sqrt{1-R^2}\left(\pi-2\sqrt{-1+\frac{1}{R^2}}-2\mathrm{ArcSin}(R)\right)}{4\pi\sqrt{-1+\frac{1}{R^2}}R}, \\ R > 0, \end{cases} \tag{23}$$

$$Sgauss^{+}{}_{i,0}(R) = \begin{cases} \frac{1}{2} - \frac{\sqrt{1-R^2}\left(-\pi+2\sqrt{-1+\frac{1}{R^2}}-2\mathrm{ArcSin}(R)\right)}{4\pi\sqrt{-1+\frac{1}{R^2}}R}, \\ R < 0, \\ \frac{\sqrt{1-R^2}\left(\pi-2\sqrt{-1+\frac{1}{R^2}}-2\mathrm{ArcSin}(R)\right)}{4\pi\sqrt{-1+\frac{1}{R^2}}R}, \\ R > 0. \end{cases} \tag{24}$$

The *'Gaussian'* part of the stress and time contributions for threshold values different from zero can be found by numerical integration. Then the analytical relations can be obtained by fitting the appropriate equation to the numerically calculated data. This procedure is applied below.

5 Results and discussion

5.1 Comparison between the '*Theoretical*' and the '*Experimental*' stress and time fractions

The *'Theoretical'* values of the flux and time fractions for each 10-min time interval are calculated using Eqs. 47–50 (Appendix A), namely the integrals of the corresponding probability distributions (Appendix A: Eqs. 38–41). By neglecting the third-order terms, these equations provide the corresponding *'Gaussian'* values. Applying the conditioning equations: Eqs. 3–5 and Eq. 7 directly to each 10-min time interval of the

Table 1 The correlation coefficient and the slope of the linear regression (in a least squares sense) between the *'Gaussian'* and *'Measured'* time (T_i) and stress (S_i) fractions, for each quadrant i, for all covariances

Gauss-measurements		T_1	T_2	T_3	T_4	S_1	S_2	S_3	S_4
$u'w'$	R^2	0.44	0.35	0.54	0.50	0.95	0.91	0.96	0.89
	Slope	0.997	0.962	1.252	1.287	0.962	1.009	1.029	0.981
$v'w'$	R^2	0.56	0.59	0.52	0.46	0.99	0.99	0.99	0.99
	Slope	1.041	1.105	1.019	0.955	0.970	0.980	0.998	0.988
$w'T'$	R^2	0.29	0.52	0.53	0.28	0.99	0.99	0.99	0.99
	Slope	0.920	1.362	1.376	0.934	1.170	1.233	0.805	0.742
$w'q'$	R^2	0.19	0.12	0.11	0.18	0.99	0.99	0.99	0.99
	Slope	1.144	0.888	0.855	1.111	1.033	1.0783	1.057	1.012

marine dataset, the corresponding *'Experimental'* or *'Measured'* values of the time and flux fractions are derived. Both *'Experimental'* and theoretically calculated quantities (*'Gaussian'* or *'Theoretical'*) of the quadrant analysis, which will be presented in the following sections, correspond to the zero threshold value ($H = 0$). The sensitivity of these quantities to the threshold value will be discussed separately.

In the first approximation, the *'Gaussian'* calculations for time and flux fractions are compared to the *'Experimental'* ones, for all covariances ($u'w'$, $v'w'$, $w'T'$and $w'q'$). The square of the correlation coefficient (R^2) and the slope of the linear regression (in a least squares sense) between the *'Gaussian'* and *'Measured'* time and stress fractions for each quadrant are summarized in Table 1. The *'Gaussian'* data represent the abscissa, while the *'Measured'* data represent the ordinate. It is apparent that scalar covariances ($w'T'$ and $w'q'$) exhibit much lower R^2 values in comparison to velocity covariances ($u'w'$ and $v'w'$) and that the correlation coefficients for the time fractions of all quadrants are significantly lower than the respective values for the flux fractions. The different functional dependence of the time and stress fractions on the correlation coefficient for a zero threshold value, which is treated in Sect. 5.2, is probably responsible for this difference. However, for thresholds around 2.5, the *'Gaussian'* distribution seems to describe almost equally the *'Experimental'* time and stress fractions, as is shown in Sect. 5.3. It is worth noting that even when the correlation coefficient is low, implying large data scattering, the slope is always close to unity, indicating that the regression well approximates the line $y(x) = x$.

In the second approximation the third-order terms (skewness and diffusion factors) for the *'Theoretical'* estimation of the time and flux fractions are taken into account, in order to increase the reliability of the calculation. Table 2 summarizes the results for all cases, and it is evident that all R^2 values are improved, while the slopes are not modified in a significant way, still retaining values around unity.

Even though the inclusion of the third-order terms clearly improve the agreement between experimental and theoretical calculations, expressed in terms of the correlation coefficient, the regression between the two datasets does not change in a significant way, well approximating the line $y(x) = x$ in all cases. Thus, one can say that the *'Experimental'* data are evenly scattered around the *'Gaussian'* pattern. These results demonstrate the necessity and even the efficiency of the third-order Gram–Charlier series in describing the time and flux contributions of each quadrant,

Table 2 The correlation coefficient and the slope of the linear regression (in a least squares sense) between the 'Theoretical' (third-order) and 'Measured' time (T_i) and stress (S_i) fractions, for each quadrant i, for all covariances

Theory (third-order)-measurements		T_1	T_2	T_3	T_4	S_1	S_2	S_3	S_4
$u'w'$	R^2	0.81	0.81	0.83	0.84	0.99	0.99	0.99	0.97
	Slope	1.154	1.158	1.181	1.158	0.984	0.985	0.994	0.975
$v'w'$	R^2	0.81	0.84	0.82	0.83	0.99	0.99	0.99	0.99
	Slope	1.041	1.048	1.085	1.148	0.971	0.982	0.997	0.986
$w'T'$	R^2	0.77	0.84	0.85	0.84	0.99	0.99	0.99	0.99
	Slope	1.266	1.013	1.038	1.156	0.993	0.999	0.979	0.970
$w'q'$	R^2	0.76	0.76	0.76	0.76	0.99	0.99	0.99	0.99
	Slope	1.284	1.383	1.406	1.279	1.042	1.045	1.048	1.045

and at the same time show the ability of the '*Gaussian*' distribution to outline the general pattern of these quantities (averaged values), but not in detail (single values).

5.2 The '*Experimental*' and the '*Gaussian*' time and flux fractions as a function of the correlation coefficient

Since the *'Gaussian'* distribution is only related to the correlation coefficient, it is natural to assume that this is the key parameter that defines the averaged values of the stress and time fractions. In fact, the usefulness of the *'Gaussian'* distribution in outlining the averaged properties of the time and stress fractions consists in its ability of enabling predictions based on a single parameter. This property will be utilized later, see Sect. 5.3. However, the fact that the scatter of the experimental data around the *'Gaussian'* value is sometimes quite large demonstrates the necessity of the '*Residual*' part of the time and/or stress fraction (Eqs. 13–16) for a more precise estimation of its exact value.

In Sects. 5.2.1 and 5.2.2 only the time and stress fractions of the $u'w'$ and the $w'q'$ covariances will be presented, as representative examples of vector and scalar fluxes, respectively, to avoid repetition. It is worth noting that these two covariances exhibit the lowest correlation coefficient of the linear regression between the *'Gaussian'* and *'Measured'* time and stress fractions, each one for its own category of flux. Thus, the largest possible data scatter is expected to arise. Also, the correlation coefficients for $w'q'$ and $v'w'$ exhibit both negative and positive *'Experimental'* values, while for $u'w'$ and $w'T'$ they exhibit only negative values, since the stable MABL data are analyzed exclusively. Therefore, the $w'q'$ covariance is offered as a study of both the negative and positive branches of the correlation coefficient.

5.2.1 The u′w′ covariance

The time fraction of each $u'w'$ quadrant (T_1, T_2, T_3 and T_4) as a function of the $u'w'$ correlation coefficient is presented in Fig. 1, where it is apparent that for increasing absolute values of the correlation coefficient, the time fraction for quadrants 2 and 4 (ejections and sweeps, respectively) increases linearly, while for quadrants 1 and 3 it decreases linearly. When the correlation coefficient's absolute value exceeds 0.3, ejections and sweeps together occupy more than 60% of the total time. There is a

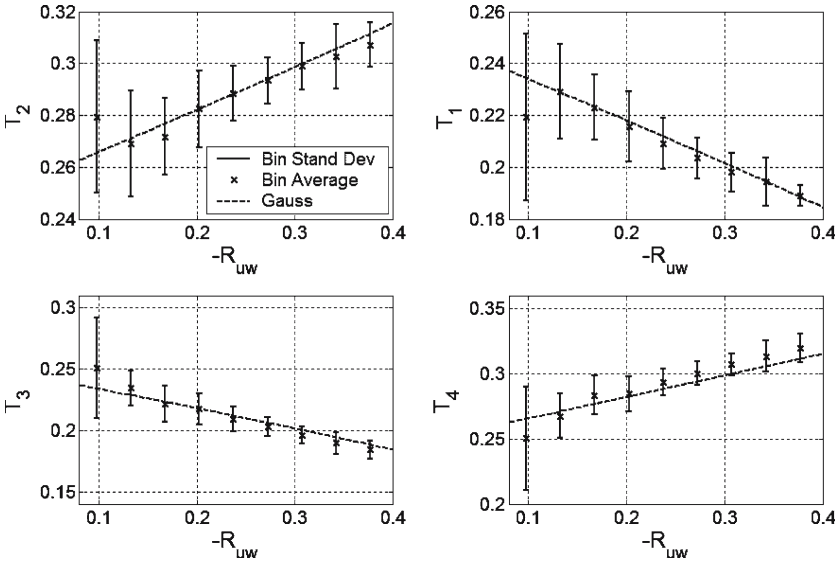

Fig. 1 The $u'w'$ time fraction of each quadrant as a function of the $u'w'$ correlation coefficient. The 'x' marks represent the bin-averaged experimental values and the error bars represent the corresponding standard deviation ($\pm\sigma$). The dotted line represents the *'Gaussian'* curve

good agreement between the *'Gaussian'* curve and the measurements for all quadrants, as already expected for averaged values of the time fraction (the *'Gaussian'* values are constantly within the range of ± 1 standard deviation). The dependence of the *'Gaussian'* time fraction on the correlation coefficient is not linear, as is apparent from Eq. 21 and Eq. 22, but for $|R| < 0.5$, it can be considered linear. The exact form of the *'Gaussian'* time fraction, as well as of the stress fraction, for the whole range of the correlation coefficient will be demonstrated in Sect. 5.3.

The flux fraction of each $u'w'$quadrant (S_1, S_2, S_3 and S_4) as a function of the $u'w'$ correlation coefficient ($-R_{uw}$) is presented in Fig. 2, where it is apparent that for increasing absolute values of the correlation coefficient, the absolute value of the flux fraction for all quadrants exponentially decreases. For large absolute values of the correlation coefficient, S_2 and S_4 asymptotically approach 0.5, while S_1 and S_3 asymptotically approach zero. Again, there is good agreement between the *'Gaussian'* curve and the bin-averaged *'Measurements'*, for all quadrants. The corresponding comparison between the *'Experimental'* data and the *'Gaussian'* predictions for the $v'w'$ covariance (not presented here) reveals that the same good agreement between the two datasets exists.

5.2.2 The $w'q'$ covariance

The $w'q'$ time and flux fractions of each quadrant as a function of the $w'q'$ correlation coefficient ($-R_{wq}$) are presented in Figs. 3 and 4 respectively.

According to Fig. 3, the agreement between the bin-averaged *'Measurements'* and the *'Gaussian'* curves of the time fractions is satisfactory for small absolute values of the correlation coefficient, while for larger values deviations are observed and the *'Gaussian'* values are hardly within the range of ± 1 standard deviation.

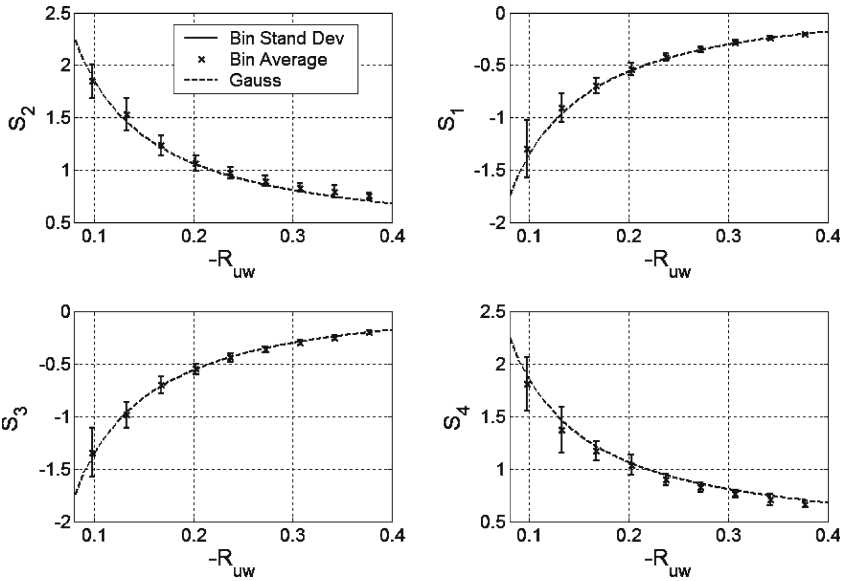

Fig. 2 The $u'w'$ flux fraction of each quadrant as a function of the $u'w'$ correlation coefficient. The 'x' marks represent the bin-averaged experimental values and the error bars represent the corresponding standard deviation ($\pm\sigma$). The dotted line represents the *'Gaussian'* curve

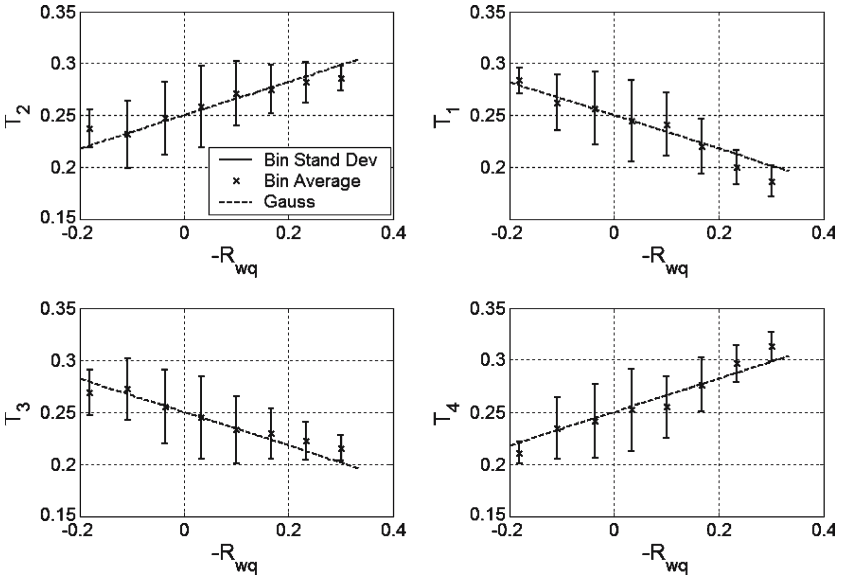

Fig. 3 The $w'q'$ time fraction of each quadrant as a function of the $w'q'$ correlation coefficient. The 'x' marks represent the bin-averaged experimental values and the error bars represent the corresponding standard deviation ($\pm\sigma$). The dotted line represents the *'Gaussian'* curve

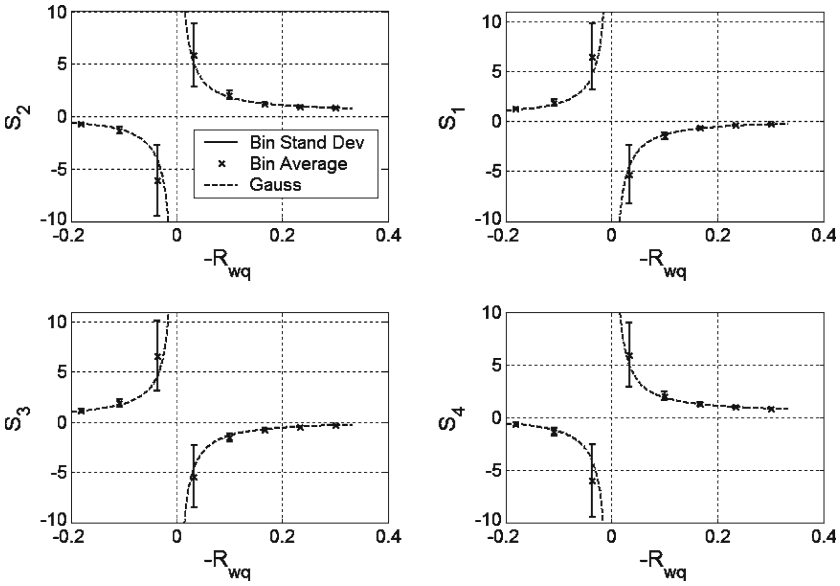

Fig. 4 The $w'q'$ flux fraction of each quadrant as a function of the $w'q'$ correlation coefficient. The 'x' marks represent the bin-averaged experimental values and the error bars represent the corresponding standard deviation ($\pm\sigma$). The dotted line represents the *'Gaussian'* curve

Regarding the flux fractions (Fig. 4), it is apparent that for increasing absolute values of the correlation coefficient the flux fraction for all quadrants decreases. For large positive values of the $-R_{wq}$ parameter, S_1 and S_3 asymptotically approach zero, while S_2 and S_4 asymptotically approach 0.5; the opposite occurs for large negative values of $-R_{wq}$. It is worth mentioning that the corresponding comparison between the *'Experimental'* data and the *'Gaussian'* predictions for the $w'T'$ covariance (not presented here) shows a similarly good agreement between the two datasets.

5.2.3 The flux exuberance

In Fig. 5 the absolute values of the exuberance (E) for the momentum and scalar fluxes, as a function of the correlation coefficient, are shown and the theoretically predicted curves are also shown (*'Gaussian'* and *'Theoretical'* values coincide in the case of the exuberance calculation due to the cancellation of the third-order terms). A good agreement between the *'Measurements'* and *'Theoretical'* calculations is evident. In the case of almost zero correlation coefficient the exuberance tends to unity, indicating an absolute balance between the upward and downward transfer.

5.3 Sensitivity of the quadrant analysis to the threshold value

In Sects. 5.1 and 5.2 the ability of the *'Gaussian'* predictions to describe the *'Experimental'* stress and time fractions was explained, for zero threshold value. In this section we examine how this ability is modified for threshold values greater than zero.

Following the methodology described in Sect. 5.1, the evaluation of the *'Gaussian'* distribution is made in terms of the correlation coefficient and the slope of the linear

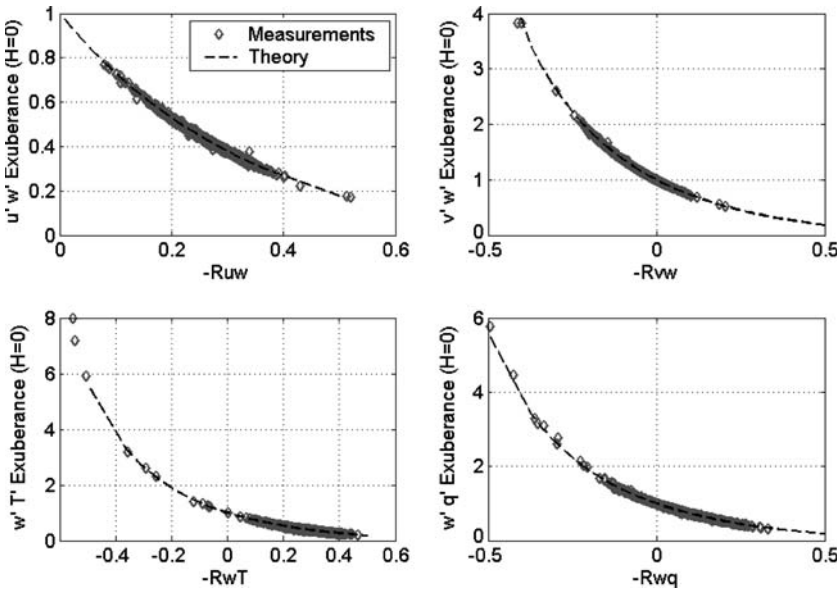

Fig. 5 Absolute value of the exuberance for momentum and scalar fluxes, as a function of the correlation coefficient. The dotted line represents the *'Theoretical'* calculation

regression (in a least squares sense) between the *'Gaussian'* and *'Experimental'* time and stress fractions. Suggestively, in Fig. 6a, the correlation coefficient and the slope of the linear regression between the *'Gaussian'* and *'Experimental'* time and stress fractions, for quadrant 2 of the $u'w'$ covariance, are depicted. It is apparent that for increasing threshold values the *'Gaussian'* predictions gradually deviate, but by a very small amount, from the *'Experimental'* stress fractions, both in terms of the correlation coefficient and the slope of the linear regression between the two samples. Regarding the time fraction slope, with the exception of the maximum value at the threshold value of 0.5, it exhibits a pattern very similar to that of the stress fraction. The most significant feature of this figure is that the time fraction R^2 increases in general from 0.35 at zero threshold value to 0.80 for a threshold of 2.5, with an exception again for a threshold value of 0.5, where a minimum value arises. Thus, the *'Gaussian'* predictions exhibit a 'local inability' in describing the *'Experimental'* time fractions for threshold values around 0.5. The *'Gaussian'* distribution seems to describe almost equally the *'Experimental'* time and stress fractions for thresholds around 2.5.

For comparison reasons, the corresponding slopes and correlation coefficients of the linear regression between the *'Theoretical'* and the *'Experimental'* data for quadrant 2 of the $u'w'$ covariance are presented in Fig. 6b. From this figure, the important role of the third-order terms (*'Theoretical'* calculations) for threshold values around 0.5, where the *'Gaussian'* approximation and the *'Experimental'* data deviate significantly (Fig. 6a), is clarified. It is important to note that the $u'w'$ covariance is constantly negative for the stable MABL data. Therefore, the above-mentioned example does not incorporate the case of positive covariance.

With the agreement between the *'Gaussian'* predictions and the *'Experimental'* data explained for threshold values from 0 to 2.5, at least for the case of negative covariance, the *'Gaussian'* predictions are now utilized in order to investigate in

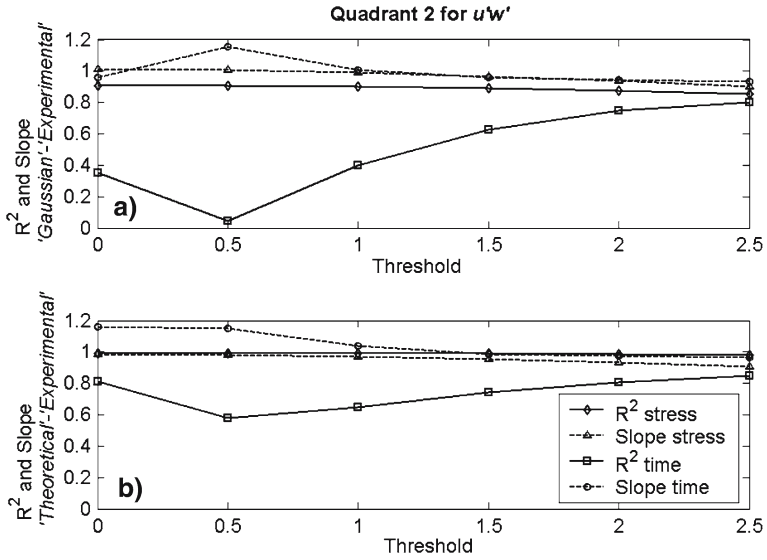

Fig. 6 (**a**) The correlation coefficient and the slope of the linear regression (in a least squares sense) between the *'Gaussian'* and *'Experimental'* time and stress fractions, for quadrant 2 of the $u'w'$ covariance. (**b**) The correlation coefficient and the slope of the linear regression (in a least squares sense) between the *'Theoretical'* and *'Experimental'* time and stress fractions, for quadrant 2 of the $u'w'$ covariance

which way the relation between the quadrant fractions (stress and time) and the correlation coefficient is modified for different threshold values. This sensitivity analysis is expanded to threshold values even greater than 2.5. More specifically, the stress and time fractions, for quadrants 1 and 2, are theoretically derived from the *'Gaussian'* distribution for 13 different threshold levels ($H = 0, 0.25, 0.5, 1, 1.5, 2, 2.5, 5, 7.5, 10, 15, 30, 45$). These values are obtained by numerical integration (*'Gaussian'* part of Eqs. 47–50, Appendix A). Of course the predictions for quadrant 1 are the same as those for quadrant 3, and the predictions for quadrant 2 are the same as those for quadrant 4. Suggestively, in Figs. 7 and 8, the *'Gaussian'* stress and time fractions respectively are plotted against the correlation coefficient, for four different threshold values. In fact, parts of the solid line corresponding to zero threshold value were also shown in Sect. 5.2 (Figs. 1–4), but only for the range of the *'Experimental'* correlation coefficients ($0.08 < -R_{uw} < 0.4$, and $-0.2 < -R_{wq} < 0.35$). It is worth noting that for negative correlation coefficients ($R < 0$) the time fractions for quadrants 2 and 4 increase for decreasing correlation coefficient ($-R$ increasing), only for small threshold values ($H < 0.5$), while for $H > 0.5$ the time fractions for quadrants 2 and 4 decrease for decreasing correlation coefficient. The transitional case of the negative correlation coefficient branches of the time fraction plots, from the increasing cases to the decreasing ones, which occurs for threshold values around 0.5, seems to directly affect the ability of the *'Gaussian'* predictions in efficiently describing the *'Experimental'* data, as was previously evident (Fig. 6a). Quadrants 1 and 3 exhibit a pattern with respect to the axis $R = 0$, which is symmetrical to that of quadrants 2 and 4.

The analytical relation for the curves appearing in Figs. 7 and 8, and for the curves that correspond to the rest of the threshold values, can be obtained by fitting the equations $\left|S_{i,H}\right| = \exp(\mathrm{a}_1 (-R)^4 + \mathrm{a}_2 (-R)^3 + \mathrm{a}_3 (-R)^2 + \mathrm{a}_4 (-R) + \mathrm{a}_5)$ and $\left|T_{i,H}\right| =$

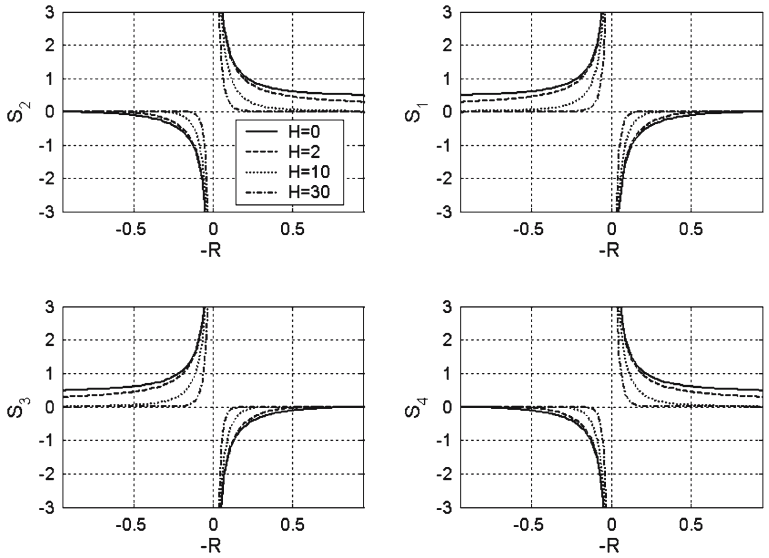

Fig. 7 The stress fraction of each quadrant, calculated from the Gaussian distribution, as a function of the correlation coefficient, for four different threshold values (H)

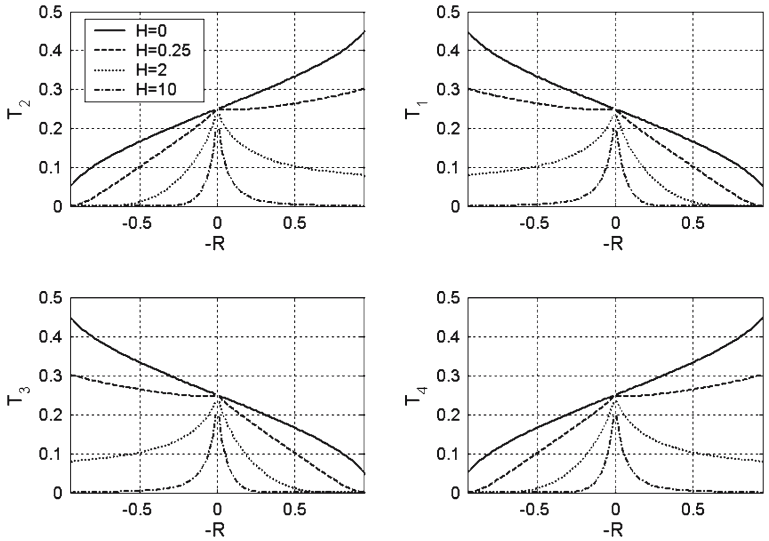

Fig. 8 The time fraction of each quadrant, calculated from the Gaussian distribution, as a function of the correlation coefficient, for four different threshold values (H)

$\exp(a_1(-R)^4 + a_2(-R)^3 + a_3(-R)^2 + a_4(-R) + a_5)$ to the numerically calculated data, except for a zero threshold value, since the analytical relation for this case is given in Eqs. 21–24. The coefficients a_i of the fourth-degree polynomial $Q(x) = a_1x^4 + a_2x^3 + a_3x^2 + ay_4x + a_5$ that fit the data $Q(-R)$ to $\ln(|S_{1,H}|)$ and to $\ln(|T_{1,H}|)$, in a least-squares sense, are summarized in Table 3. It should be mentioned that the

Table 3 The coefficients a_i of the fourth degree polynomial $Q(x) = a_1x^4 + a_2x^3 + a_3x^2 + a_4x + a_5$ that fits the data $Q(-R)$ to $\ln(|S_{1,H}|)$ and to $\ln(|T_{1,H}|)$, in a least-squares sense

H	$-0.7 < -R < -0.1$					$0.1 < -R < 0.7$				
	a_1	a_2	a_3	a_4	a_5	a_1	a_2	a_3	a_4	a_5
Flux fraction S_1										
0.25	18.588	37.916	30.107	11.943	1.518	11.507	−31.36	26.764	−14.493	1.482
0.5	18.515	37.772	30.009	11.974	1.5192	6.8736	−26.446	24.329	−14.116	1.4584
1	18.323	37.398	29.785	12.083	1.5233	−2.6079	−16.436	19.165	−13.383	1.4117
1.5	18.108	36.994	29.578	12.244	1.529	−12.126	−6.3316	13.839	−12.694	1.3665
2	17.893	36.605	29.412	12.446	1.536	−21.72	3.9192	8.4116	−12.041	1.3224
2.5	17.688	36.247	29.289	12.683	1.5437	−31.329	14.203	2.9694	−11.427	1.2794
5	16.89	35.018	29.263	14.207	1.5884	57.199	−130	72.597	−27.895	2.3301
7.5	16.428	34.539	29.925	16.066	1.6349	−137.7	158.66	−82.248	1.5018	0.26608
10	16.204	34.565	31.009	18.103	1.6796	−360.5	457.69	−226	25.52	−1.2936
15	16.221	35.558	33.919	22.469	1.7605	−365.47	385.77	−168.81	3.7178	0.16866
30	14.241	36.279	42.341	35.924	1.9105	−405.31	311.36	−134.87	−19.973	0.83261
45	45.978	91.891	80.968	55.832	2.4059	−814.58	833.17	−427.25	25.093	−3.1874
Time fraction T_1										
0.25	0.36284	0.76616	0.71774	0.080097	−1.3981	−6.6152	6.2272	−3.1989	−0.8323	−1.431
0.5	0.64481	1.4479	1.4209	0.608	−1.409	−11.244	10.764	−5.3492	−0.98773	−1.4656
1	1.1402	2.6175	2.631	1.5119	−1.4288	−20.354	19.808	−9.6601	−1.1482	−1.5325
1.5	1.5723	3.6322	3.6926	2.3151	−1.4469	−29.45	28.917	−14.033	−1.2034	−1.5978
2	1.9631	4.5494	4.6623	3.0612	−1.4636	−38.519	38.031	−18.433	− 1.2025	−1.6616
2.5	2.3206	5.3928	5.5651	3.7687	−1.4794	−47.667	47.285	−22.924	−1.1501	−1.7251
5	3.8113	8.9526	9.4912	6.9889	−1.5483	30.391	−68.084	27.519	−13.938	−1.2119
7.5	5.0127	11.888	12.874	9.9387	−1.606	−328.53	442.39	−226.86	32.523	−4.4688
10	6.0497	14.472	15.961	12.752	−1.6567	−368.41	452.89	−215.77	23.66	−3.9488
15	7.8658	19.079	21.658	18.168	−1.7431	−207.43	132.7	−34.348	−22.208	−1.2673
30	33.726	69.556	60.407	38.966	−1.5646	−483.12	461.58	−237.06	8.1415	−5.0223
45	31.067	53.307	48.195	45.123	−2.5062	−952.39	1064.7	−561.7	55.893	−9.1524

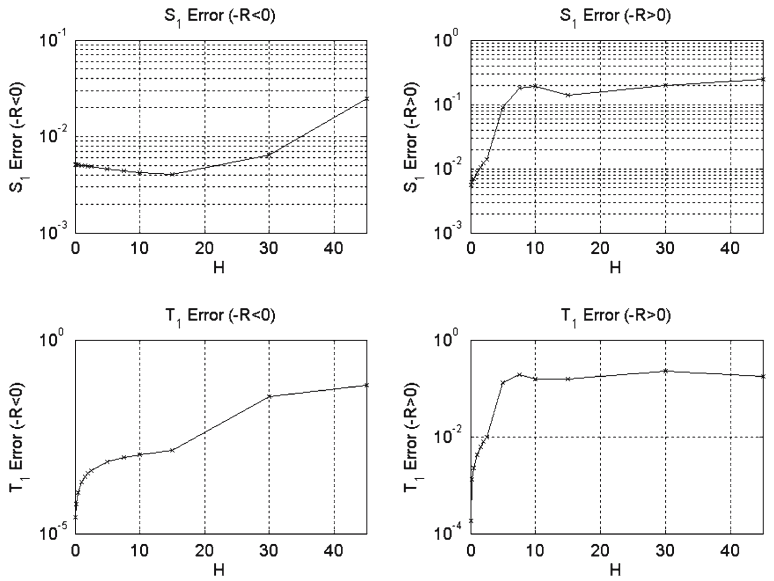

Fig. 9 The errors for the estimated stress and time fractions, as a function of the threshold value (H), for the first quadrant

least-squares fit is only applied to the data in the range $0.1 < |R| < 0.7$, since expanding the fit to a greater range is problematic, at least for the fourth-degree polynomial. Besides, the experimental correlation coefficient values do not exceed 0.7 for all covariances.

The coefficients in Table 3 refer only to the first quadrant. The following relations describe the coefficients that correspond to the other three quadrants:

a_i(quadrant 2, $-R < 0$) = a_i(quadrant 1, $-R > 0$), i = 1, 3, 5
a_i(quadrant 2, $-R < 0$) = $-a_i$(quadrant 1, $-R > 0$), i = 2, 4
a_i(quadrant 2, $-R > 0$) = a_i(quadrant 1, $-R < 0$), i = 1, 3, 5
a_i(quadrant 2, $-R > 0$) = $-a_i$(quadrant 1, $-R < 0$), i = 2, 4
a_i(quadrant 3) = a_i(quadrant 1), i = 1, 2, 3, 4, 5
a_i(quadrant 4) = a_i(quadrant 2), i = 1, 2, 3, 4, 5.

The errors (Err) that occur for the estimated stress and time fraction logarithms, as a function of the threshold value, by making use of the above-mentioned equations, are presented in Fig. 9, at least for the first quadrant.

The interval ±Err around the estimated values corresponds to a 50% confidence interval, while the interval ±2Err corresponds to a 95% confidence interval. The errors for the other quadrants can be described as follows:

Error(quadrant 2, $-R < 0$) = Error(quadrant 1, $-R > 0$),
Error(quadrant 2, $-R > 0$) = Error(quadrant 1, $-R < 0$),
Error(quadrant 3) = Error(quadrant 1),
Error(quadrant 4) = Error(quadrant 2).

Even though these errors are a function of the correlation coefficient, they can be considered fairly constant, at least for the range $0.2 < |R| < 0.6$. In Fig. 9 the mean

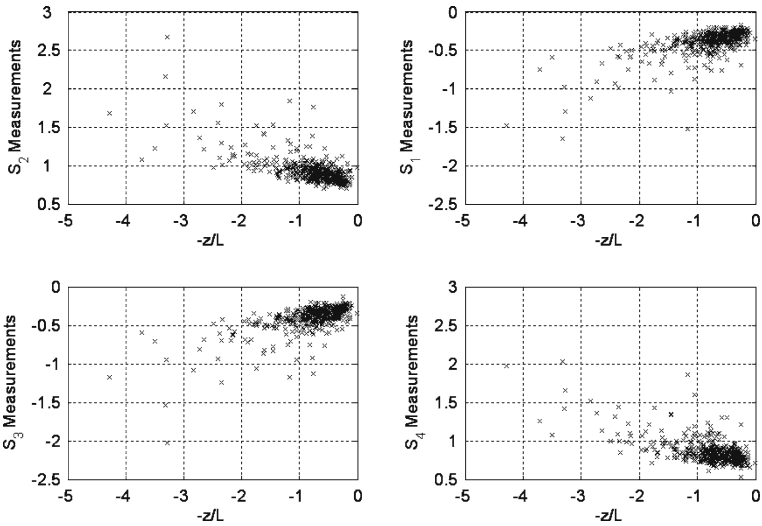

Fig. 10 Stress fractions of all quadrants as a function of the stability parameter $(-z/L)$

errors for the whole range of the correlation coefficient are considered for each threshold value. It is important to note that the a_i coefficients have been obtained for the logarithm of the absolute values of the stress and time fractions. Thus, when using the analytical calculations for the time and stress fractions with the above-mentioned coefficients, the proper sign of these quantities should be considered. More specifically, the quantities $S_1(-R > 0)$, $S_2(-R < 0)$, $S_3(-R > 0)$ and $S_4(-R < 0)$ should be considered negative. With the above relations, the analytical relations earlier presented are somehow completed. Using these relations in combination with Eqs. 13–16 and Eqs. 21–24, one can predict the flux and time contributions of each quadrant and for all covariances for a wide range of threshold and correlation coefficient values.

5.4 Sensitivity of the quadrant analysis to the stability parameter

Here, the dependence of the stress and time fractions on the stability is examined. Only the $u'w'$ covariance, for zero threshold value is examined. As a measure of the stability the parameter $-z/L$ (defined in Sect. 3) is used. The value of z/L for the stable MABL dataset ranges from 4.3 (very stable conditions) to 0.003 (near-neutral conditions). The flux fraction absolute value for all quadrants decreases for decreasing z/L (towards neutral conditions), as shown in Fig. 10, while the time fraction for quadrants 2 and 4 increases and for quadrants 1 and 3 decreases (not shown).

In analogy to the exuberance for the flux fractions (Eq. 8), the corresponding quantity for the time fractions can be defined by using the time fractions ($T_{i,H}$) instead of the stress fractions ($S_{i,H}$) in Eq. 8. The time and flux exuberances as a function of the stability parameter are presented in Fig. 11, where it is apparent that correlated and uncorrelated motions tend to balance for increasingly stable conditions, probably due to turbulence suppression and the elimination of larger-scale eddies under strong stratification. Towards neutral conditions the prevalence of the correlated motions is evident in terms of both time and stress contributions. Substantially, these results

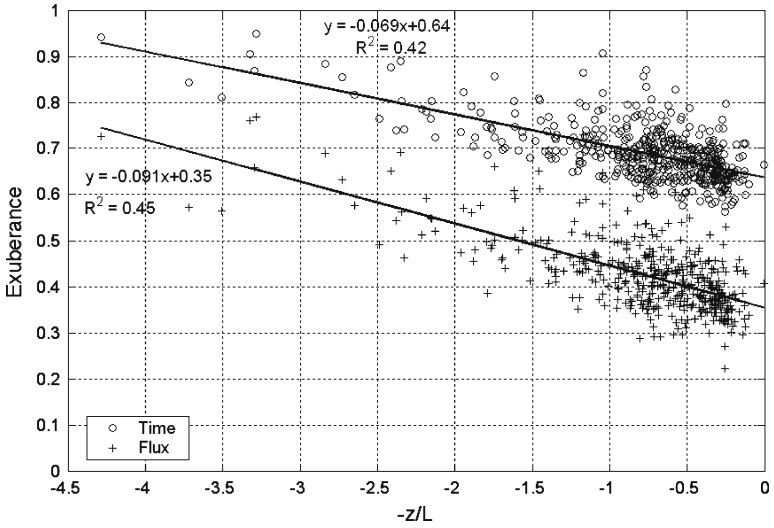

Fig. 11 The time and flux exuberance as a function of the stability parameter $(-z/L)$. The equations and the correlation coefficients (R^2) correspond to a linear fit in a least squares sense to the two datasets

reflect the sensitivity upon stability of the $u'w'$ correlation coefficient, which has been identified as a key parameter in the quadrant analysis. More specifically, the $u'w'$ correlation coefficient gradually increases from values less than 0.1 for very stable conditions to more than 0.35 for near-neutral conditions (not shown).

5.5 Sensitivity of the quadrant analysis to the local averaging scale

The preceding quadrant analysis is exclusively based on the fluctuating components of the scalar and momentum transport from 10-min averages (Reynolds averaging length). In this section the sensitivity of the analysis to the choice of the averaging length is examined. For this purpose the $u'w'$ covariance from two different MABL datasets, one stationary and the other non-stationary, is analyzed for eight different averaging time scales: 0.5, 1, 2, 5, 10, 20, 30 and 60 minutes, for zero threshold value ($H = 0$). The stationary and non-stationary cases were defined according to the methodology described by Mahrt et al. (1996), and the classification as stationary or non-stationary was based on the ratio:

$$\beta = \frac{\left(\sigma_u^2 + \sigma_v^2\right)^{\frac{1}{2}}}{\overline{U}}, \tag{25}$$

where the standard deviations are computed from the six 10-min averages of the wind components for a 1-h period and $\overline{U}$ is the 1-h averaged wind speed. If the hourly value of β exceeds 0.1, the case is identified as non-stationary.

The absolute value of the stress fraction for all quadrants increases for increasing averaging length and this increase is much more evident for the non-stationary class (Fig. 12).

The time fraction for quadrants 2 and 4 decreases with increasing time scales, while for quadrants 1 and 3 it increases, for both stationary and non-stationary cases (not shown). However, the variation is slightly more intense for the non-stationary class.

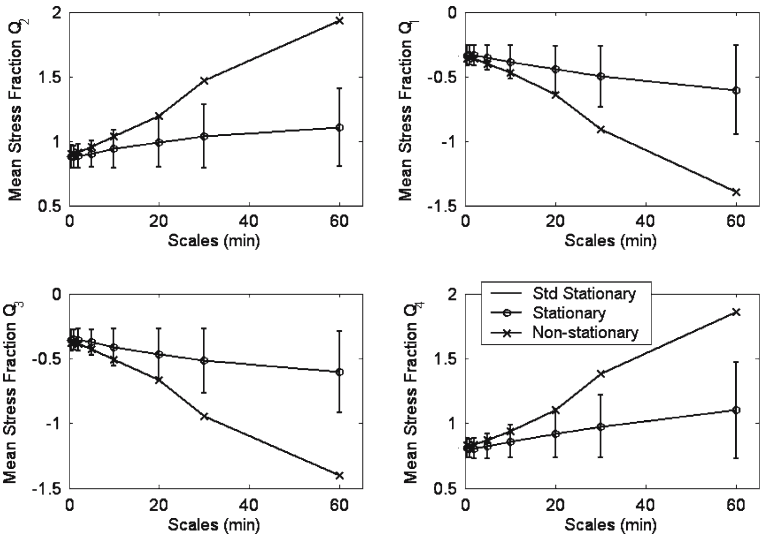

Fig. 12 Mean stress fraction of all quadrants as a function of the Reynolds averaging scale, for a stationary and a non-stationary dataset. The error bars represent the corresponding standard deviations ($\pm\sigma$). Error bars for the non-stationary class are not shown for clarity reasons

For example, in the case of stationary data, the mean time fraction for quadrant 2 decreases from 0.295 at the 0.5-min scale to 0.287 at the 60-min scale and for the non-stationary case the corresponding mean values are 0.292 and 0.273, respectively.

The absolute value of the mean exuberance (E) for the flux and time fractions as a function of the averaging scale is presented in Fig. 13, for both the stationary and non-stationary classes. It is apparent that the exuberance increases for increasing time scales in all cases, but slightly more rapidly for the non-stationary cases. This behaviour indicates that for large time scales the inclusion of wave-like motions in the analysis produces a more balanced contribution of the four quadrants to the total stress and time, while for small time scales, which correspond to turbulence, the contribution of quadrants 2 and 4 becomes more evident. The quite large data scatter, indicated by the standard deviations, is associated with the inclusion of all the stable marine cases in the analysis, which exhibit a wide range of correlation coefficient values. Since the exuberance is driven by the correlation coefficient (Fig. 5) this scatter is predictable. The same applies for the standard deviations of the stress and time fractions, because these quantities mainly depend on the correlation coefficient (but also on the skewness and diffusion factors), as was shown at Sect. 5.2.

6 Conclusions

The quadrant analysis for momentum and scalar fluxes was applied to stable MABL data from the CBLAST-Low, Nantucket experiment.

The theoretical stress and time contributions of each quadrant to the total stress was calculated by making use (integrating) of (a) the Gaussian probability distribution, and (b) the conditional Gram–Charlier expansion of the Gaussian distribution

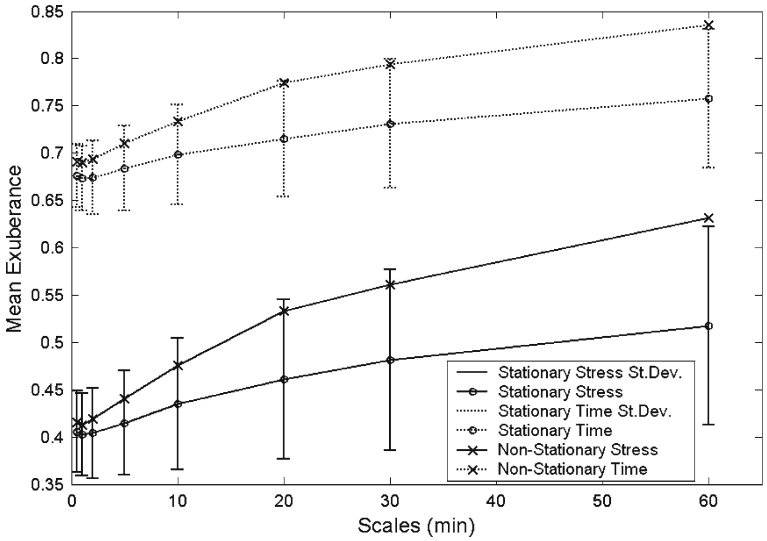

Fig. 13 Absolute value of the flux and time mean exuberance as a function of the Reynolds averaging scale, for a stationary and a non-stationary dataset. The error bars represent the corresponding standard deviations ($\pm\sigma$). Error bars for the non-stationary class are not shown for clarity reasons

up to the third-order terms. Comparison with the experimental data showed that the third-order Gram–Charlier series was necessary and even sufficient in most of the cases, in describing the time and flux contributions of each quadrant, for both scalar and momentum transport, while the ability of the Gaussian distribution is limited to outlining the general pattern of these quantities. In fact the Gaussian distribution exhibited good reliability in describing the averaged values of stress and time fractions of all quadrants, as a function of the correlation coefficient. This property was very useful, since it enabled predictions based on a single parameter. However, the Gaussian distribution by predicting a symmetrical pattern between the diagonal quadrants becomes incapable of describing the intermittent turbulent diffusion process. This process is related to the third-order terms of the Gram–Charlier series.

The sensitivity of the Gaussian stress and time fractions of each quadrant on the choice of the threshold value, which separates the most important events from the less significant ones, was evident not only qualitatively, but in some cases also quantitatively. More specifically, the dependence of the time fraction on the correlation coefficient reverses sign when the threshold value crosses 0.5. This fact affects the ability of the *'Gaussian'* predictions in efficiently describing the *'Experimental'* data for threshold values around 0.5.

Finally, the sensitivity of the $u'w'$ covariance for zero threshold value on the atmospheric stability and the Reynolds averaging scales showed that correlated and uncorrelated motions tend to balance for increasingly stable conditions or for large time scales, due to the inclusion of wave-like motions in the analysis, while towards neutral conditions or for small time scales corresponding to turbulence, the prevalence of the correlated motions is evident in terms of both time and stress contributions.

Acknowledgements This work was co-financed within Op. Education by the ESF (European Social Fund) and National Resources, the Office of Naval Research and the University of Athens.

Appendix A: The probability distribution of the Gram–Charlier type

In order to quantify the departures of the joint probability density distributions of turbulent velocities from Gaussianity, we consider the joint probability distribution of the Gram–Charlier type, which involves the following Hermite polynomials of two variables (Frenkiel and Klebanoff 1967):

$$H_{j,k}(x,y) = (-1)^{j+k}\, \mathrm{e}^{\frac{1}{2}\Phi(x,y)} \frac{\partial^{j+k}}{\partial x^j \partial y^k}\, \mathrm{e}^{-\frac{1}{2}\Phi(x,y)}, \tag{26}$$

$$G_{j,k}(x,y) = (-1)^{j+k}\, \mathrm{e}^{\frac{1}{2}\Psi(x,y)} \frac{\partial^{j+k}}{\partial x^j \partial y^k}\, \mathrm{e}^{-\frac{1}{2}\Psi(x,y)}, \tag{27}$$

where

$$\Phi(\hat{u},\hat{w}) = \frac{\hat{u}^2 - 2R\hat{u}\hat{w} + \hat{w}^2}{1-R^2}, \tag{28}$$

$$\Psi(\xi,\zeta) = \xi^2 + 2R\xi\zeta + \zeta^2 \tag{29}$$

with

$$\xi = \frac{\hat{u} - R\hat{w}}{1-R^2}, \tag{30a}$$

$$\zeta = \frac{\hat{w} - R\hat{u}}{1-R^2}, \tag{30b}$$

In the above-mentioned equations R is the correlation coefficient, defined as:

$$R = \frac{\overline{u'w'}}{\sigma_u \sigma_w}, \tag{31}$$

and

$$\hat{u} = \frac{u'}{\sigma_u}, \tag{32a}$$

$$\hat{w} = \frac{w'}{\sigma_w}, \tag{32b}$$

are the velocity fluctuations normalized by the corresponding standard deviation. Then the joint probability density distribution is given by

$$P(\hat{u},\hat{w}) = P_0(\hat{u},\hat{w}) \sum_{j+k=0}^{j+k=n} A_{j,k} H_{j,k}(\hat{u},\hat{w}) \tag{33}$$

with

$$A_{j,k} = \frac{1}{j!k!} \overline{G_{j,k}\left(\hat{u},\hat{w}\right)}, \tag{34}$$

and

$$P_0(\hat{u},\hat{w}) = \frac{1}{2\pi(1-R^2)^{\frac{1}{2}}} \exp\left(-\frac{\hat{u}^2 - 2R\hat{u}\hat{w} + \hat{w}^2}{2(1-R^2)}\right), \tag{35}$$

where P_0 is the Gaussian distribution for two variables. Thus, Eq. 33 represents the expansion of the probability P around the Gaussian probability. By making use

of Eqs. 27 and 34 we obtain the first 10 coefficients $G_{j,k}$ and $A_{j,k}$ that correspond to a third-order expansion of the distribution (for $j+k<4$): $G_{00}=1$, $G_{01}=\hat{w}$, $G_{10}=\hat{u}$, $G_{11}=-R+\hat{u}\hat{w}$, $G_{02}=-1+\hat{w}^2$, $G_{20}=-1+\hat{u}^2$, $G_{30}=\hat{u}\left(-3+\hat{u}^2\right)$, $G_{03}=\hat{w}\left(-3+\hat{w}^2\right)$, $G_{21}=-2R\hat{u}+\left(-1+\hat{u}^2\right)\hat{w}$, $G_{12}=-2R\hat{w}+\left(-1+\hat{w}^2\right)\hat{u}$ and $A_{00}=1$, $A_{01}=A_{10}=A_{11}=A_{02}=A_{20}=0$, $A_{30}=M_{30}/6$, $A_{03}=M_{03}/6$, $A_{21}=M_{21}/2$, $A_{12}=M_{12}/2$, where $M_{j,k}=\overline{\hat{u}^j\hat{w}^k}$ is the (j,k) moment of the distribution. The third-order expansion is sufficient in describing the time and flux contributions of each quadrant, for both scalar and momentum transport, so higher order terms are ignored. Moreover, for the fourth-order expansion some parts of the probability density distribution exhibit negative values and thus make the use of this expansion limited (Frenkiel and Klebanoff 1967). The third-order Gram–Charlier distribution can be written as:

$$P(\hat{u},\hat{w})=P_0(\hat{u},\hat{w})\left[1+\sum_{j+k=3}^{3}\frac{M_{jk}}{j!k!}H_{jk}(\hat{u},\hat{w})\right]. \tag{36}$$

If all the third-order moments are equal to zero, Eq. 36 provides the Gaussian distribution. Nakagawa and Nezu (1977) obtained this special form of the Gram–Charlier distribution by making use of the cumulant expansion method, for the two variables u' and w'. Then, by using a conditional calculation the contribution to the Reynolds stress from each quadrant of the quadrant analysis can be predicted. Defining the normalized Reynolds stress as:

$$\omega=\frac{\hat{u},\hat{w}}{\overline{u',w'}} \tag{37}$$

the probability distributions of each quadrant can be described by the following relations (by considering a negative sign for the correlation coefficient:$R=-\frac{\overline{u'w'}}{\sigma_u\sigma_w}$):

$$\begin{aligned}P_1(\omega)=&\frac{R}{2\pi}\,\mathrm{e}^{Rt}\frac{K_0(|t|)}{(1-R^2)^{\frac{1}{2}}}+\frac{R}{2\pi}\,\mathrm{e}^{Rt}K_{\frac{1}{2}}(|t|)\frac{|t|^{\frac{1}{2}}}{(1+R)^2}\\&\left[(1+R)\left(\frac{S^+}{3}+D^+\right)|t|-\left(\frac{2-R}{3}S^++D^+\right)\right],\end{aligned} \tag{38}$$

$$\begin{aligned}P_2(\omega)=&\frac{R}{2\pi}\,\mathrm{e}^{Rt}\frac{K_0(|t|)}{(1-R^2)^{\frac{1}{2}}}+\frac{R}{2\pi}\,\mathrm{e}^{Rt}K_{\frac{1}{2}}(t)\frac{t^{\frac{1}{2}}}{(1+R)^2}\\&\left[(1-R)\left(\frac{S^-}{3}+D^-\right)t-\left(\frac{2+R}{3}S^-+D^-\right)\right],\end{aligned} \tag{39}$$

$$\begin{aligned}P_3(\omega)=&\frac{R}{2\pi}\,\mathrm{e}^{Rt}\frac{K_0(|t|)}{(1-R^2)^{\frac{1}{2}}}-\frac{R}{2\pi}\mathrm{e}^{Rt}K_{\frac{1}{2}}(|t|)\frac{|t|^{\frac{1}{2}}}{(1+R)^2}\\&\left[(1+R)\left(\frac{S^+}{3}+D^+\right)|t|-\left(\frac{2-R}{3}S^++D^+\right)\right],\end{aligned} \tag{40}$$

$$\begin{aligned}P_4(\omega)=&\frac{R}{2\pi}\,\mathrm{e}^{Rt}\frac{K_0(|t|)}{(1-R^2)^{\frac{1}{2}}}-\frac{R}{2\pi}\,\mathrm{e}^{Rt}K_{\frac{1}{2}}(t)\frac{t^{\frac{1}{2}}}{(1+R)^2}\\&\left[(1-R)\left(\frac{S^-}{3}+D^-\right)t-\left(\frac{2+R}{3}S^-+D^-\right)\right],\end{aligned} \tag{41}$$

where

$$S^{+} = \frac{1}{2}(S_w + S_u) = \frac{1}{2}(Q_{03} + Q_{30}) = \frac{1}{2}\left(\overline{\hat{w}^3} + \overline{\hat{u}^3}\right), \tag{42}$$

$$S^{-} = \frac{1}{2}(S_w - S_u) = \frac{1}{2}(Q_{03} - Q_{30}) = \frac{1}{2}\left(\overline{\hat{w}^3} - \overline{\hat{u}^3}\right), \tag{43}$$

$$D^{+} = \frac{1}{2}(D_u + D_w) = \frac{1}{2}(Q_{21} + Q_{12}) = \frac{1}{2}\left(\overline{\hat{w}\hat{u}^2} + \overline{\hat{u}\hat{w}^2}\right), \tag{44}$$

$$D^{-} = \frac{1}{2}(D_u - D_w) = \frac{1}{2}(Q_{21} - Q_{12}) = \frac{1}{2}\left(\overline{\hat{w}\hat{u}^2} - \overline{\hat{u}\hat{w}^2}\right), \tag{45}$$

$$t \equiv \frac{R\omega}{(1 - R^2)}. \tag{46}$$

Here, S_u and S_w are the skewness factors of u and w respectively, D_u and D_w correspond to turbulent diffusion in the x and z directions respectively, and K_v is the V-order modified Bessel function of the second kind. The following relations describe the time fraction $T_{i,H}$ and the flux or stress fraction $S_{i,H}$ of each quadrant:

$$T_{i,H} = \int_{H}^{\infty} P_i(\omega)\, \mathrm{d}\omega, \tag{47}$$

for $i = 2, 4$,

$$T_{i,H} = \int_{-\infty}^{-H} P_i(\omega)\, \mathrm{d}\omega, \tag{48}$$

for $i = 1, 3$,

$$S_{i,H} = \int_{H}^{\infty} \omega P_i(\omega)\, \mathrm{d}\omega, \tag{49}$$

for $i = 2, 4$,

$$S_{i,H} = \int_{-\infty}^{-H} \omega P_i(\omega)\, \mathrm{d}\omega, \tag{50}$$

for $i = 1, 3$.

The total probability density function is given by

$$P(\omega) = P_1(\omega) + P_2(\omega) + P_3(\omega) + P_4(\omega) = \left(\frac{R}{\pi}\right) \mathrm{e}^{Rt} \frac{K_0(|t|)}{(1 - R^2)^{\frac{1}{2}}}. \tag{51}$$

Figure 14a gives $P(\omega)$ for different correlation coefficient values, while the probability distribution of the Reynolds stress ($\omega P(\omega)$) is shown in Fig. 14b. The total probability is independent of the skewness and diffusion factors due to cancellation of the terms that include the third-order cumulants. The positive tails of $P(\omega)$ are larger than the negative ones since:

$$\overline{\omega} = \int_{-\infty}^{\infty} \omega P(\omega) \mathrm{d}\omega = 1. \tag{52}$$

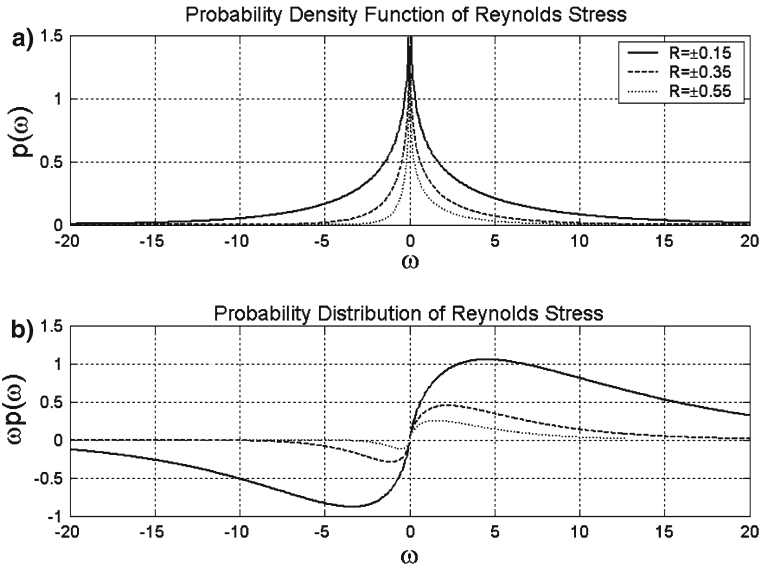

Fig. 14 (**a**) The total probability density function of the Reynolds stress $P(\omega)$, for 3 different correlation coefficient values. (**b**) The probability distribution of the Reynolds stress ($\omega P(\omega)$)

References

Antonia RA (1981) Conditional sampling in turbulence measurements. Ann Rev Fluid Mech 13:131–156

Begstrom H, Hogstrom U (1989) Turbulent exchange above a pine forest II: organized structures. Boundary-Layer Meteorol 49:231–263

Bogard DG, Tiederman WG (1986) Burst detection with single-point velocity measurements. J Fluid Mech 162:389–413

Boppe RS, Neu WL (1995) Quasi-coherent structures in the marine atmospheric surface layer. J Geophys Res 100(C10):20635–20648

Boppe RS, Neu WL, Shuai H (1999) Large-scale motions in the marine atmospheric surface layer. Boundary-Layer Meteorol 92:165–183

Cantwell B (1981) Organized motion in turbulent flow. Ann Rev Fluid Mech 13:457–515

Frenkiel F, Klebanoff P (1967) Higher order correlations in a turbulent field. Phys Fluids 10:507–520

Hogstrom U, Bergstrom H (1996) Organized turbulence structures in the near-neutral atmospheric surface layer. J Atmos Sci 53:2452–2464

Katul G, Kuhn G, Schieldge J, Hsieh C-I (1997) The ejection-sweep character of scalar fluxes in the unstable surface layer. Boundary-Layer Meteorol 83:1–26

Mahrt L, Vickers D, Howell J, Hojstrup J, Wilczak J, Edson J, Hare J (1996) Sea surface drag coefficients in the Riso Air Sea Experiment. J Geophys Res 101(C6):14,327–14,335

Maitani T, Ohtaki E (1987) Turbulent transport process of momentum and sensible heat in the surface layer over paddy field. Boundary-Layer Meteorol 40:283–293

Maitani T, Shaw RH (1990) Joint probability analysis of momentum and heat fluxes at deciduous forest. Boundary-Layer Meteorol 52:283–300

Nagakawa H, Nezu I (1977) Prediction of the contributions to the Reynolds stress from bursting events in open-channel flows. J Fluid Mech 80:99–128

Raupach MR (1981) Conditional statistics of Reynolds stress in rough-wall and smooth-wall turbulent boundary layers. J Fluid Mech 108:363–382

Robinson SK (1991) Coherent motions in the turbulent boundary layer. Ann Rev Fluid Mech 23:601–639

Shaw RH (1985) On diffusive and dispersive fluxes in forest canopies. In: Hutchinson BA, Hicks BB (eds) The forest-atmosphere interaction. D. Reidel Publishing Company, Dordrecht, pp 407–419

Shaw RH, Tavangar J, Ward DP (1983) Structure of Reynolds stress in a canopy layer. J Clim Appl Meteorlol 22:1922–1931

Wang Q, Helmis CG, Gao Z, Kalogiros J, Wang S (2004) Variations of boundary layer mean and turbulence structure using synthesized observations. 16th symposium on boundary layers and turbulence, 9–14 August, Portland, ME. (http://ams.confex.com/ams/pdfpapers/78415.pdf)

Willmarth WW, Lu SS (1974) Structure of the Reynolds stress and the occurrence of bursts in the turbulent boundary layer. Adv Geophys 18A:287–314